


**Extended computation of the viscous Rayleigh-Taylor instability in a horizontally confined flow**Jon Martinez-Carrascal , J. Calderon-Sanchez, and L. M. González-Gutiérrez*School of Naval Engineering, Universidad Politécnica de Madrid (UPM), Avda. de la Memoria 4, 28040 Madrid, Spain*

A. de Andrea González

*Departamento de Física, Escuela Politécnica Superior, Universidad Carlos III de Madrid, Av. Universidad 30, 28911 Leganés, Spain*

(Received 17 March 2021; accepted 5 May 2021; published 28 May 2021)

In this article, the classical Rayleigh-Taylor instability is extended to situations where the fluid is completely confined, in both the vertical and horizontal directions. This article starts with the two-dimensional (2D) viscous periodic case with finite height where the effect of adding surface tension to the interface is analyzed. This problem is simulated from a dual perspective: first, the linear stability analysis obtained when the Navier-Stokes equations are linearized and regularized in terms of density and viscosity; and second, looking at the weakly compressible version of a multiphase smoothed particle hydrodynamics (WCSPH) method. The evolution and growth rates of the different fluid variables during the linear regime of the SPH simulation are compared to the computation of the eigenvalues and eigenfunctions of the viscous version of the Rayleigh-Taylor stability (VRTI) analysis with and without surface tension. The most unstable mode, which has the maximal linear growth rate obtained with both approaches, as well as other less unstable modes with more complex structures are reported. The classical horizontally periodic (VRTI) case is now adapted to the case where two additional left and right walls are included in the problem, representing the cases where a two-phase flow is confined in a accelerated tank. This 2D case where no periodic assumptions are allowed is also solved using both techniques with tanks of different sizes and a wide range of Atwood numbers. The agreement with the linear stability analysis obtained by a Lagrangian method such as multiphase WCSPH is remarkable.

DOI: [10.1103/PhysRevE.103.053114](https://doi.org/10.1103/PhysRevE.103.053114)**I. INTRODUCTION**

In many aircraft models, the fuel is transported inside tanks placed along the wing structures. Due to the great extreme accelerations on the aircraft wings, violent fluid movement and strong impacts with the tank walls are produced. This complex fluid phenomenon is known as sloshing [1]. In the analysis of vertically excited sloshing cases, violent sloshing is of great interest for airplane manufacturers, where very interesting hydrodynamic phenomena are found, such as the free surface instabilities that appear at the first stages of the movement. These instabilities are an extended version of Rayleigh-Taylor instabilities, where fluid properties such as viscosity and surface tension play a role.

Normally the Rayleigh-Taylor instability (RTI) appears when a heavy fluid overlies a lighter fluid [2,3] and gravity is oriented towards the light fluid; in other words, the density gradient and gravity are opposed. This situation is present in a wide variety of applications: ferrofluids [4], tectonics [5], exploding foils [6], aerobreakup [7], and astrophysics [8,9]. An original extension of the RTI appears in the sloshing phenomena when two different fluids are confined in a accelerated tank. In this case, the light fluid overlies a heavier fluid when gravity is present, but the RTI appears when a larger acceleration than gravity is applied to both fluids in the opposite direction to the force of gravity. As explained before, the density gradient is opposed to the difference between the inertial force and gravity.

Mikaelian [10] analyzed the Rayleigh-Taylor instability in two finite-thickness fluids taking viscosity effects into account. A numerical dispersion relation was obtained for different thicknesses and Atwood numbers. He performed a one-dimensional (1D) analysis based on two fluids separated with a sharp interface using homogeneous Dirichlet and Neumann conditions for the velocity at the top and bottom boundaries and compatibility conditions at the interface. The two-dimensional (2D) extension presented in this work allows the analysis of more complex flows and includes the possibility of studying diffuse interfaces, the sharp interface being just a particular case.

Obied Allah [11] investigated the finite-thickness effect of a slab of incompressible fluid with exponentially increasing density supported by a fluid of constant density in the presence of surface tension. He found that the finite thickness has a stabilizing effect on the RTI.

Morgan *et al.* [12] studied the behavior of the most unstable VRTI mode initiated with a diffuse interface. The results exhibit good agreement with the dynamic diffusion model of Duff *et al.* [13] for small wave numbers, but produces larger growth rates for large wave number perturbations.

Yu *et al.* [14] investigated the inviscid RTI for a fluid with an hyperbolic tangent density distribution. They obtained the multiple eigenvalues for the growth rates of the RTI and the corresponding eigenfunctions which may have potential applications in comprehending the mixing behavior existing in many areas. Moreover, they obtained a fitting expression

for those eigenmodes in the dimensionless form, which agrees well with the numerical results for limited Atwood numbers  $A_\rho \leq 0.8$ . Dong *et al.* [15] revisited the physical problem that was studied in [14] by developing a short-wavelength asymptotic solution. Based on the Wentzel-Kramers-Brillouin (WKB) approximation, the growth rates of the RTI were obtained for Atwood numbers close to unity.

However, to the best of our knowledge no numerical study on the eigenvalue problem associated with the VRTI in a confined tank has been performed. Therefore, we need to carry out this research study in the case of 2D geometries where the no-slip boundary conditions are imposed on the top and bottom walls but also on the lateral walls. Similarly to [16], a hyperbolic tangent distribution for the density and viscosity profiles is imposed, which allows skipping the compatibility conditions when sharp interfaces are simulated. Starting with the additional step introduced by the presence of the lateral walls, the development of the RTI inside more complex geometries, for example, including intermediate vertical baffles, could also be studied using the same methodology.

In order to confirm the findings, the VRTI is also reproduced using the meshless Lagrangian method smoothed particle hydrodynamics (SPH), which is gaining significant attention in recent decades according to its ability to deal with complex physics and complex geometries, such as the field of fluid dynamics involving free-surface flows. SPH exhibits significant advantages when compared to other methods, such as finite elements or finite volumes when dealing with multiphase flow, because density is transported by the particles and there is no need to include an additional scalar transport equation. The transport of scalar functions by advection equations performed in formulations such as volume of fluid (VOF) or level set is not a numerically trivial problem that normally implies dispersion and diffusion numerical errors and loss of interface sharpness. This particular situation where multiphase formulation is compulsory seems to be a perfect opportunity to test the modern and robust WCSPH version presented in [17]. Most of the literature addressing the Rayleigh-Taylor problem with SPH normally focuses on the evolution of the flow and the robustness of the numerical formulation, but very few authors compare the growth rates with other results from the stability analysis. Some of the first attempts correspond to Refs. [18,19], using incompressible (ISPH) and weakly compressible (WCSPH) approaches respectively. Works on multiphase SPH developed by Ref. [20], [21], or [22] present results for the Rayleigh-Taylor problem to validate their different multiphase SPH or surface tension formulations, but these are analyzed only from a qualitative perspective in terms of free-surface evolution at certain characteristic instants in time.

A further step is performed in [23], where some comparison with approximate solutions of the classical stability analysis is performed. In contrast to the work presented here, the initial free surface is deformed instead of initialized with a velocity field. In that study, a quantitative analysis of the growth rate of the VRTI in a confined geometry is carried out for a single instability mode and a single Atwood number. The analysis focuses on the dependence of the problem with the surface tension.

In this paper the following ideas are proposed: first, a general 2D formulation is presented to analyze the RTI that considers the possibility of using density-and viscosity-regularized fluids, geometrical flexibility, alternative boundary conditions, and surface tension implementation. In particular, the possibility of using no-slip lateral boundary conditions allows for the analysis of a completely confined tank, and also the quantification of the differences with the well-known periodic VRTI spectrum. Finally, we want to confirm that a meshless Lagrangian numerical method such as WCSPH is able to reproduce the dynamics observed in this particular multiphase problem with reasonable accuracy.

The paper is organized as follows: in Sec. II the general description to the RTI is explained and the general equations are presented. In Sec. III both solution methodologies, the linear stability analysis and the SPH formulation, are detailed. In Sec. IV the results obtained by both methodologies for the VRTI problem with different boundary conditions are monitored and compared. Finally, conclusions are presented in Sec. V.

## II. PROBLEM SETUP

The strategies to perform the linear stability analysis are presented in this section. To study the viscous version of the Rayleigh-Taylor instability, we assume a zero velocity base flow and regularized density and viscosity distributions that represent two fluids separated by a common interface. We analyze the evolution of the perturbations by the assumed base flow. In particular, we are interested in the development of two-dimensional flow structures and the growth rates of the different unstable modes. The calculations have been performed in a 2D computational domain. Previous validations of the viscous and inviscid cases without surface tension in 1D and 2D geometries can be found in [16].

Let  $\rho_1, \mu_1, \nu_1$  and  $\rho_2, \mu_2, \nu_2$  be the densities and the kinematic and dynamic viscosities of the top (heavy) and bottom (light) fluids, respectively. The two-phase flow is governed by the incompressible Newtonian Navier-Stokes equations in a domain  $\Omega$  in the presence of gravity  $g$ , which imply mass and momentum conservation, and a density transport equation. As the velocity base flow is zero, the viscosity transport equation is not necessary in this VRTI formulation; see [24]. The domain will be a rectangle of height  $2H$  and width  $2L$  contained on the  $XY$  plane, mathematically expressed as  $\Omega = [-L, L] \times [-H, H]$ .

Similarly to [25], the characteristic time, length, velocity, pressure, density, and viscosity scales used to transform the problem to its nondimensional version are defined as

$$\rho_o = \frac{\rho_1 + \rho_2}{2}, \quad \mu_o = \frac{\mu_1 + \mu_2}{2}, \quad \nu_o = \frac{\nu_1 + \nu_2}{2}, \quad (1)$$

$$t_o = (\nu_o/g^2)^{1/3}, \quad l_o = (\nu_o^2/g)^{1/3}, \quad u_o = (g\nu_o)^{1/3}, \quad (2)$$

$$k_o = (\nu_o^2/g)^{-1/3}, \quad p_o = \rho_o g (\nu_o^2/g)^{1/3}. \quad (3)$$

The nondimensional version of this set of equations reads

$$\rho \frac{\partial \mathbf{u}}{\partial t} + \rho \mathbf{u} \cdot \nabla \mathbf{u} = -\nabla p + \rho \mathbf{u}_g + \nabla[\mu(\nabla \mathbf{u} + \nabla \mathbf{u}^T)], \quad (4)$$

$$\nabla \cdot \mathbf{u} = 0, \quad (5)$$

$$\frac{\partial \rho}{\partial t} + \mathbf{u} \cdot \nabla \rho = 0, \quad (6)$$

where  $\rho$ ,  $\mathbf{u}$ ,  $p$ ,  $t$ ,  $\nabla$ ,  $\mu$ ,  $\tau$ ,  $\mathbf{u}_g$  are the nondimensional density, velocity, pressure, time, nabla operator, viscosity, viscous stress tensor, and unity vector representing gravity.

A steady nonparallel basic flow  $(\bar{u}_i, \bar{\rho}, \bar{p})$  is perturbed by small-amplitude velocity  $\tilde{u}_i$ , density  $\tilde{\rho}$ , and pressure  $\tilde{p}$  perturbations, as follows:

$$u_i(x, y, z, t) = \bar{u}_i(x, y) + \varepsilon \tilde{u}_i(x, y, z, t) + \text{c.c.}, \quad (7)$$

$$p(x, y, z, t) = \bar{p}(x, y) + \varepsilon \tilde{p}(x, y, z, t) + \text{c.c.}, \quad (8)$$

$$\rho(x, y, z, t) = \bar{\rho}(x, y) + \varepsilon \tilde{\rho}(x, y, z, t) + \text{c.c.}, \quad (9)$$

where  $\varepsilon \ll 1$ , and c.c. denotes the conjugate of the complex quantities  $\tilde{u}_i$ ,  $\tilde{\rho}$ , and  $\tilde{p}$ . As base flow, we consider two superposed fluids at rest  $\bar{u}_i = 0$  separated by a regularized interface at  $y = 0$  and subjected to a constant gravitational acceleration pointing downwards the vertical direction  $y$ .

Therefore, in order to describe the Rayleigh-Taylor (RT) instability of a sharp interface, it seems more consistent to attempt to solve the problem for a transition layer of finite thickness, and then take the limit when the thickness tends to zero. Similarly to the sharp jump implementation used in [16], we adopt the density and viscosity profiles

$$\bar{\rho} = 1 + A_\rho \tanh(y/L_s), \quad \mu = 1 + A_\mu \tanh(y/L_s), \quad (10)$$

where  $L_s$  is the gradient scale length of the density and viscosity layers and  $A_\rho, A_\mu$  the Atwood numbers given by

$$A_\rho = \frac{\rho_1 - \rho_2}{\rho_1 + \rho_2}, \quad A_\mu = \frac{\mu_1 - \mu_2}{\mu_1 + \mu_2}. \quad (11)$$

Taking account of Eqs. (10), typical air-water hydrodynamic instabilities in the presence of a sharp interface can be recovered by setting  $L_s \rightarrow 0$ . When Eqs. (7), (8), and (9) are substituted into the Navier-Stokes equations (4), (5), and 6, assuming zero base flow  $\bar{u}_i = 0$  and neglecting second-order terms, the linearized Navier-Stokes equations for the perturbation quantities are obtained:

$$\bar{\rho} \frac{\partial \tilde{u}_i}{\partial t} = -\frac{\partial \tilde{p}}{\partial x_i} + \mu \Delta \tilde{u}_i + \left( \frac{\partial \tilde{u}_j}{\partial x_i} + \frac{\partial \tilde{u}_i}{\partial x_j} \right) \frac{\partial \mu}{\partial x_j} + \tilde{\rho} u_{gi} \quad (12)$$

$$\frac{\partial \tilde{\rho}}{\partial t} + \tilde{u}_j \frac{\partial \bar{\rho}}{\partial x_j} = 0, \quad (13)$$

$$\frac{\partial \tilde{u}_i}{\partial x_i} = 0. \quad (14)$$

Since the coefficients of  $\tilde{u}_i$ ,  $\tilde{\rho}$ , and  $\tilde{p}$  do not depend on  $z$  and  $t$ , the perturbation quantities can be written as normal modes:

$$\tilde{u}_i(x, y, z, t) = \hat{u}_i(x, y) e^{ik_z z} e^{\gamma t} + \text{c.c.}, \quad (15a)$$

$$\tilde{p}(x, y, z, t) = \hat{p}(x, y) e^{ik_z z} e^{\gamma t} + \text{c.c.}, \quad (15b)$$

$$\tilde{\rho}(x, y, z, t) = \hat{\rho}(x, y) e^{ik_z z} e^{\gamma t} + \text{c.c.}, \quad (15c)$$

where the complex conjugate (c.c.) is required to render the perturbations real. Additionally,  $\gamma = \sigma + i\omega \in \mathbb{C}$  is the complex growth or decay rate  $\sigma$  and oscillation frequency  $\omega$ .

Let us add the presence of the surface tension on the free surface that separates both fluid phases to this perturbed system. Following [25], the surface tension presence adds the term  $-2(\partial_{xx}\hat{\xi}_s - k_z^2\hat{\xi}_s)S\delta_s(y - y_s)$  to the  $y$  projection of Eq. (12). Here  $\hat{\xi}_s = \hat{\xi}(x, y_s)e^{k_z z}e^{\gamma t}$  is the vertical displacement of the free surface at  $y = y_s$ ,  $\delta_s(y - y_s)$  is the Dirac's  $\delta$  function, and  $S$  is the nondimensional surface tension, which can be expressed as

$$S = \frac{T_s}{(\rho_1 + \rho_2)(g\nu^4)^{1/3}}, \quad (16)$$

where  $T_s$  is the dimensional surface tension. In order to proceed with the numerical integration, the Dirac  $\delta$  function will be regularized and the term  $\hat{\xi}$  can be related to the vertical velocity perturbation  $\hat{v}$  as

$$\hat{v} = \frac{\partial \hat{\xi}}{\partial t} = \gamma \hat{\xi}. \quad (17)$$

In Sec. III, a 2D variational formulation of the equations using a second-order finite element discretization is performed. A Taylor-Hood triangular element where the density perturbation was also approximated by second-order polynomials is used to solve the linearized Navier-Stokes equations around the base flow; see [26] for details.

### III. MATHEMATICAL MODELS

#### A. Linear stability: 2D eigenvalue-problem formulation and solution methodology

We are particularly interested in the temporal stability analysis on a 2D computational domain ( $k_z = 0$ ). The fluids are confined in the vertical direction, and consequently homogeneous Dirichlet boundary conditions are used on the top and bottom boundaries  $y = \pm H$ . On the right and left boundaries  $x = \pm L$  either periodic boundary conditions (periodic configuration) or homogeneous Dirichlet boundary conditions (tank configuration) will be used; see both configurations in Fig. 1. Consequently, this framework does not contain any explicit  $z$ -coordinate. A 3D generalization of this framework, where the perturbations assume a spanwise periodic length (i.e., homogeneous direction) and  $L_z$  is defined through the real wave number  $k_z = \frac{2\pi}{L_z} \in \mathbb{R}$  is performed in [26].

In the classical 1D instability analysis of the VRTI, a periodic solution with unlimited wavelength in both the horizontal  $x$  and spanwise  $z$  directions [14] is assumed. In the periodic boundary case (see the top part of Fig. 1), the BiGlobal EVP [27] represented by Eqs. (12)–(14) has been solved without the explicit assumption of the periodic structure in the horizontal  $x$  direction, but with limited wavelength for the computed eigenvectors in the horizontal direction  $k_x > \frac{\pi}{L}$  and infinite spanwise length. For the horizontally confined case studied here (see the bottom part of Fig. 1), no periodicity assumption is possible, and the 2D formulation is compulsory.

Substitution of the ansatz (15) into the perturbation equations (12)–(14) yields

$$-\mu \nabla^2 \hat{u} + \frac{\partial \hat{p}}{\partial x} - \frac{d\mu}{dy} \left( \frac{\partial \hat{v}}{\partial x} + \frac{\partial \hat{u}}{\partial y} \right) = -\gamma \bar{\rho} \hat{u}, \quad (18)$$

$$-\mu \nabla^2 \hat{v} + \frac{\partial \hat{p}}{\partial y} - 2 \frac{d\mu}{dy} \frac{\partial \hat{v}}{\partial y} + \hat{\rho} - 2(\partial_{xx}\hat{\xi})S\delta_s(y - y_s) = -\gamma \bar{\rho} \hat{v}, \quad (19)$$

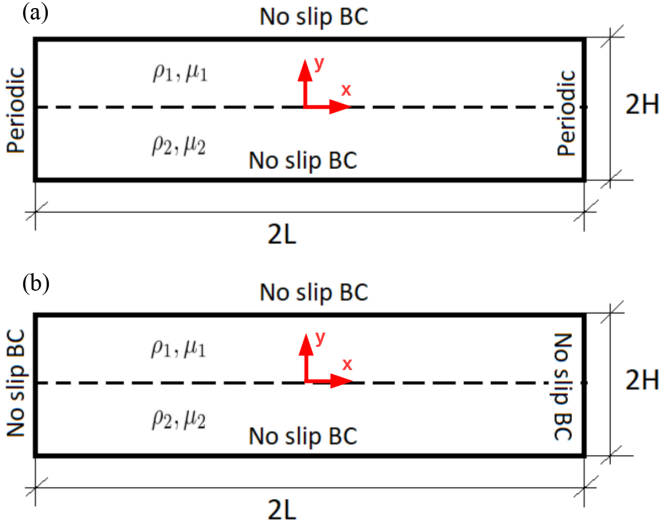


FIG. 1. Schemes of the computational geometry used for the Rayleigh-Taylor simulations. A dashed line at  $y=0$  indicates the interface between fluids. The boundary conditions are also written at each boundary for both cases: periodic (a) and tank (b) configurations.

$$-\mu \nabla^2 \hat{w} - \frac{d\mu}{dy} \left( \frac{\partial \hat{w}}{\partial y} \right) = -\gamma \bar{\rho} \hat{w}, \quad (20)$$

$$\hat{v} \frac{d\bar{\rho}}{dy} = -\gamma \hat{\rho}, \quad (21)$$

$$\frac{\partial \hat{u}}{\partial x} + \frac{\partial \hat{v}}{\partial y} = 0, \quad (22)$$

where  $\nabla^2$  is the Laplacian operator limited to our  $XY$  2D domain. As the present study is 2D,  $k_z = 0$ , the eigenvalue problem given by Eqs. (18)–(22) is real. As consequence, the projection of the momentum equation (20) on the  $Z$  direction is the only one that contains the velocity perturbation component  $\hat{w}$  and can be decoupled from the rest. This system can be simplified from six to five differential equations, eliminating the vertical displacement  $\hat{\xi}$ . Combining Eqs. (21) and (17) the free surface perturbation can be related to the density perturbation as

$$\hat{\xi} = -\frac{1}{\frac{d\bar{\rho}}{dy}} \hat{\rho}. \quad (23)$$

We also express the Dirac  $\delta$  function regularized as

$$\delta_s(y - y_s) = \frac{1}{2A_\rho} \frac{d\bar{\rho}}{dy}. \quad (24)$$

This converts system (18)–(22) into a real generalized eigenvalue problem:

$$A \cdot \mathbf{X} = -\gamma B \cdot \mathbf{X}, \quad (25)$$

where  $\mathbf{X} = (\hat{u}, \hat{v}, \hat{w}, \hat{\rho}, \hat{p})^T$  with real linear operators  $A$  and  $B$  that can be expressed as

$$A = \begin{pmatrix} \mathcal{L} & -\frac{d\mu}{dy} \partial_x & 0 & 0 & \partial_x \\ 0 & \mathcal{L} - \frac{d\mu}{dy} \partial_y & 0 & 1 + \frac{s}{A_\rho} \partial_{xx} & \partial_y \\ 0 & 0 & \mathcal{L} & 0 & 0 \\ 0 & \frac{d\bar{\rho}}{dy} & 0 & 0 & 0 \\ \partial_x & \partial_y & 0 & 0 & 0 \end{pmatrix} \quad (26)$$

being the operator  $\mathcal{L}$

$$\mathcal{L} = -\mu \nabla^2 - \frac{d\mu}{dy} \partial_y, \quad (27)$$

where the matrix  $B$

$$B = \begin{pmatrix} \bar{\rho} & 0 & 0 & 0 & 0 \\ 0 & \bar{\rho} & 0 & 0 & 0 \\ 0 & 0 & \bar{\rho} & 0 & 0 \\ 0 & 0 & 0 & 1 & 0 \\ 0 & 0 & 0 & 0 & 0 \end{pmatrix}. \quad (28)$$

The boundary conditions for the lateral periodic boundaries are

$$\hat{u}(-L, y) = \hat{u}(L, y), \quad (29)$$

$$\hat{v}(-L, y) = \hat{v}(L, y), \quad (30)$$

$$\hat{u}(x, \pm H) = 0, \quad (31)$$

$$\hat{v}(x, \pm H) = 0; \quad (32)$$

when no-slip lateral boundaries at  $x = \pm L$  are used, conditions (29) and (30) are both equal to zero.

In general, the eigenvalues  $\gamma$  of such a real eigenvalue problem are either real, or they arise as pairs of complex conjugate eigenvalues. Adopting the existing nomenclature from the literature (see, e.g., Theofilis *et al.* [28]), the corresponding eigenvectors describe either stationary modes ( $\gamma = 0$ ) or traveling waves ( $\gamma = \pm i\omega \neq 0$ ).

To discretize the equations, we use a triangular-element-based unstructured mesh. The eigenvalue problem is solved using the Arnoldi method based on a Krylov-subspace iteration, originally proposed in [29] and discussed in detail in [27]. In order to check the accuracy of the results during the stability analysis, the number of mesh nodes was increased until three significant digits of the most unstable eigenvalue converged.

In the case that the horizontal periodicity is assumed in the whole domain, the problem could be reduced to the 1D formulation; see [16] for details. In that case, the problem could be solved by the quadratic eigenvalue problem for the vertical velocity perturbation  $\hat{v}$ :

$$(A\gamma^2 + B\gamma + C)\hat{v} = 0, \quad (33)$$

where operators  $A$  and  $B$  are identical to the ones in [16] and operator  $C$  changes due to the surface tension term as follows:

$$C = -k^2 \frac{d\bar{\rho}}{dy} \left( I - k^2 \frac{S}{A_\rho} \right), \quad (34)$$

where  $k$  is the wave number associated with the assumed horizontal periodicity.

### B. SPH formulation

One of the objectives of this work is to prove that the SPH formulation is a valid tool to perform a stability analysis of the VRTI. For that purpose, we are going to discretize the set of equations (4) using the multiphase  $\delta$ -WCSPH formulation detailed in [17]. The software used is AQUA<sub>gpusph</sub> [30], an open source SPH code based on GPU capabilities. The discretized set of equations reads

$$\frac{dV_i}{dt} = V_i(\mathbf{u}_i - \mathbf{u}_j) \cdot \nabla W_{ij} V_i + \delta h c_{0\chi} \sum_{j \in \chi} \mathbf{D}_{ij}^V \cdot \nabla W_{ij} V_j, \quad (35)$$

$$\begin{aligned} \rho_i \frac{d\mathbf{u}_i}{dt} = & - \sum_j (p_i + p_j) \nabla W_{ij} V_j + \rho_i \mathbf{g} \\ & + \mu_\chi \sum_{j \in \chi} \pi_{ij} \nabla W_{ij} V_j + \mathbf{\Omega}, \end{aligned} \quad (36)$$

$$\frac{d\mathbf{r}_i}{dt} = \mathbf{u}_i, \quad (37)$$

$$\rho_i = \sum_{j \in \chi} m_j W_{ij}^S, \quad (38)$$

$$p_i = \frac{\rho_{0\chi} c_{0\chi}^2}{\gamma_\chi} \left[ \left( \frac{\rho_i}{\rho_{0\chi}} \right)^{\gamma_\chi} - 1 \right] + p_b. \quad (39)$$

This set of equations is composed of a volume conservation equation (35), a momentum conservation equation (36), a time evolution of the trajectory of each particle (37), an evaluation of the density field (38), and an equation of state (39). Here  $V_j$  accounts for the volume of the neighbor particles  $j$ , and  $W_{ij} = W(\mathbf{r}_j - \mathbf{r}_i, h)$  and  $\nabla_i W_{ij} = \nabla W(\mathbf{r}_j - \mathbf{r}_i, h)$  represent the kernel function and its derivative with respect to the  $i$ th particle, at constant  $h$ , respectively. In this work, a Wendland C2 kernel with  $h/dr = 2$  is used, where  $h$  and  $dr$  correspond to the smoothing length and the particle distance, respectively. The dissipation effects due to viscosity are modeled through the function  $\pi_{ij}$ , which is defined as

$$\pi_{ij} = \frac{(\mathbf{u}_j - \mathbf{u}_i) \cdot (\mathbf{r}_j - \mathbf{r}_i)}{\|\mathbf{r}_j - \mathbf{r}_i\|^2}. \quad (40)$$

In the volume conservation equation, an additional term is added to avoid spurious high-frequency pressure oscillations, following the work in [31] and extended to the multiphase formulation in [17]. An additional term of this form has actually become a standard in SPH, and this particular model is the so-called  $\delta$ -SPH. The term  $\mathbf{D}_{ij}^V$  is defined as

$$\begin{aligned} \mathbf{D}_{ij}^V = & V_i \left[ 2 \left( 1 - \frac{\rho_j}{\rho_i} \right) - \frac{1}{\rho_i} ((\nabla \rho)_j^L + (\nabla \rho)_i^L) \cdot (\mathbf{r}_j - \mathbf{r}_i) \right] \\ & \times \frac{(\mathbf{r}_j - \mathbf{r}_i)}{\|\mathbf{r}_j - \mathbf{r}_i\|^2}, \end{aligned} \quad (41)$$

where  $(\nabla \rho)_i^L$  represents the renormalized density gradient, as defined in [32]. The value for  $\delta$  is set always to 0.1, following the value used in [33] based on the study carried out in [31]. Note that the sum of the neighbors is extended to neighboring particles of the same phase  $j \in \chi$ .

In the momentum conservation equation,  $\rho$  is the fluid density,  $\mathbf{g}$  represents the gravity,  $\mathbf{\Omega}$  the surface tension force,  $p$  the pressure, and  $\mu_\chi$  the dynamic viscosity of phase  $\chi$ . The flow velocity,  $\mathbf{u}$ , is defined as the material derivative of a fluid particle position,  $\mathbf{r}$ .

In order to close the system of equations in (35)–(38) a stiff equation of state (39) is needed. In this work a polytropic equation of state is used where  $\gamma_\chi$  is the polytropic exponent of phase  $\chi$ ,  $\rho_{0\chi}$  represents the reference density of phase  $\chi$ , and  $p_b$  represents the background pressure that is set to  $p_b = 1$  Pa in all simulations presented in this work. The compressibility of the phase can be adjusted artificially by changing the speed of sound of the phase  $c_{0\chi}$  [34].

As the continuity equation is expressed in terms of volume, density is evaluated with a summation formula (38) within phase  $\chi$ . According to this, the kernel  $W_{ij}^S$  is defined for each phase as

$$W_{ij}^S = \frac{W_{ij}}{\sum_{k \in \chi} W_{ik} V_k}. \quad (42)$$

Time integration is performed by means of a predictor-corrector scheme [30]. The Courant-Friedrichs-Lewy (CFL) condition is set to 0.1 to ensure time stability.

When surface tension is taken into account an additional term  $\mathbf{\Omega}$  is added to the momentum equation in Eq. (36) to deal with effects at the interface. This force has been included in SPH in the same fashion as in [35], and the expression reads

$$\mathbf{\Omega} = -\frac{T_s}{\rho_i} \sum_j (\mathbf{n}_j - \mathbf{n}_i) \cdot \nabla W_{ij} V_j \mathbf{n}_i, \quad (43)$$

where  $T_s$  is the surface tension coefficient and  $\mathbf{n}_i$  represents the local normal vector to the interface of particle  $i$ .

Both periodical and wall boundary conditions are set in the corresponding numerical tests carried out in this work.

Periodical boundary conditions are defined such that every generic field  $f$  satisfies

$$f(x)|_{\partial\Omega_1} = f(x)|_{\partial\Omega_2}. \quad (44)$$

For wall boundary conditions, either slip or no-slip conditions can be imposed.

Boundary integral methodology is used in this work. The formulation employed here is based on the work in [36] solving these numerically as explained in [30] with the semi-analytical expressions for the kernel obtained in [37] based on [38]

No-slip boundary conditions are imposed at the discrete level in the same fashion as described in [39] for the boundary integrals formulation, such that

$$\left\langle \frac{\partial \mathbf{u}}{\partial \mathbf{n}} \right\rangle = \sum_{j \in BE} \left[ \frac{(\mathbf{I} - \mathbf{n}_j \otimes \mathbf{n}_j) \mathbf{u}_{ji}}{|\mathbf{r}_{ij} \cdot \mathbf{n}_j|} \right] W_{ij} V_i S_j. \quad (45)$$

**IV. RESULTS**

The generalized eigenvalue problem given by expression (25) is numerically solved using the respective boundary conditions. The solution of this problem gives the dominant eigenvalues and their corresponding eigenfunctions. In parallel, the corresponding SPH simulations are also completed with the same parameters, and both results are compared in this section.

First, as the preliminary case, we will solve the viscous 2D Rayleigh-Taylor stability analysis problem with periodic lateral boundary conditions and surface tension. The results will be compared to the well-known 1D solution found in the literature.

Hereafter, we will compare the growth rate obtained as being the largest eigenvalue of the linear stability analysis with the growth rate of the velocity interpolation in a fixed point of the SPH simulation. The comparison will be performed for several Atwood numbers, a wide range of wave numbers, and typical surface tension values.

The completely confined problem, where the lateral boundary conditions will be changed to the no-slip case, is solved by both methodologies. This problem is motivated by the VRTI that appears during the first stage of a vertically accelerated fuel tank typically found in the transport industry. In this particular confined case, the discussion about the meniscus shape and the contact angle will be avoided by assuming no surface tension in the fluid, and consequently the initial SPH and the base flow interfaces will both be flat everywhere. In this case the dominant part of spectrum and the corresponding eigenvectors obtained after the solution of the eigenvalue problem will be compared for both types of lateral boundary conditions. This change of the spectrum confirms the importance of the 2D formulation, capable of implementing both boundary conditions. This problem will be fully simulated with SPH, and the growth rate of the linear part also will be compared to the results of the eigenvalue problem.

**A. VRTI with surface tension and periodic lateral boundary conditions**

*1. Linear stability analysis*

In the present section, a linear stability analysis will be performed for the VRTI when the surface tension is added to the problem and quantified by the parameter  $S$ . This complete 2D analysis (dominant eigenvalue spectrum and corresponding eigenvectors are computed) includes viscosity, surface tension, and finite height and periodic width. Regarding this, we should mention that [10] determined an approximated analytical expression of the dispersion relation for the 1D case that included viscosity, surface tension, and finite height, but no eigenvector was represented. The nondimensional dispersion relation can be expressed as

$$\sigma = -k^2 + \sqrt{k^4 - k(k^2S - A_\rho) \tanh(kH)}, \quad (46)$$

which gives good results for large wave numbers. All the computations are performed in a computational domain  $H = 1$  and  $L = 4$ . The number of quadratic mesh nodes and

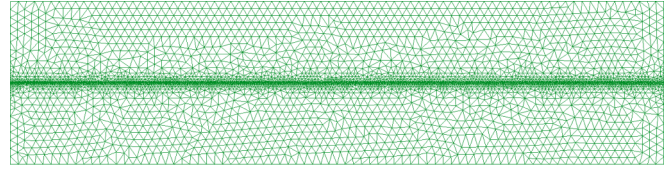


FIG. 2. Mesh used for the 2D viscous simulation.

triangular elements is 23 145 and 11 458, respectively, where the mesh has been refined around the  $x$  axis; see Fig. 2.

In Figs. 3 and 4 the growth rate has been represented for  $L_s = 0.01$  and  $H = 1$  as a function of the wave number  $k$  for two different cases: the first with  $A_\rho = A_\mu = 0.2$  and  $S = 0.003$ , and the second with larger density and viscosity gradients  $A_\rho = A_\mu = 0.6$  and more surface tension  $S = 0.01$ . In both cases, the dispersion relation for the 1D spectral Chebyshev formulation previously presented in [16], but adding the surface tension term as indicated at the end of Sec. III A, was also computed solving the quadratic eigenvalue problem. These results were included as a reference in order to confirm the accuracy of the current 2D formulation and to evaluate the effect of the surface tension in the problem. Similarly, in the case without surface tension (see [16]), all density and viscosity ratios computed present a local maximum that increases with the Atwood number. It can be observed (see Fig. 10 in [16]) that the higher the Atwood number, the larger the difference between the computed value in 2D and the reference value obtained in the 1D case due to numerical errors caused by the discretization of the density gradient.

In Fig. 5 the amplitude perturbations corresponding to the eigenvalue are represented for all the fluid variables for an interface scale length  $L_s = 0.01$ . The horizontal periodicity of the structure is clearly observable. The wave number is obtained after measuring the wave length of the structure  $\lambda_x = 2$  in the picture, and then computing the wave number as  $k = 2\pi/\lambda_x = \pi$ .

*2. SPH simulation of the VRTI*

In this section the VRTI will be simulated using the nonlinear SPH multiphase formulation; see Sec. III B. Most

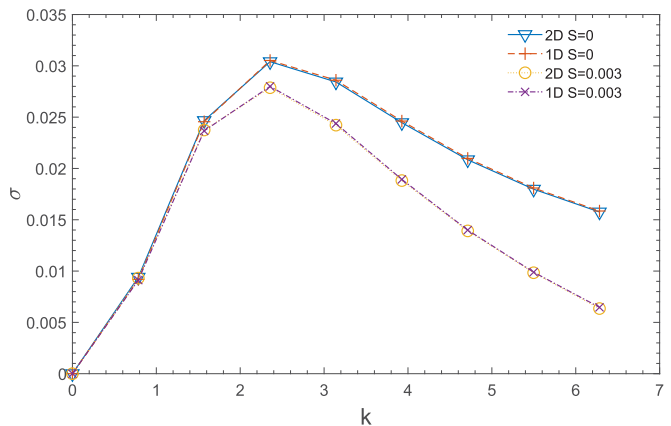


FIG. 3. Growth rate instability as a function of the wave number, for  $A_\rho = A_\mu = 0.2$ ,  $L_s = 0.01$ ,  $H = 1$ ,  $S = 0$ , and  $S = 0.003$ .

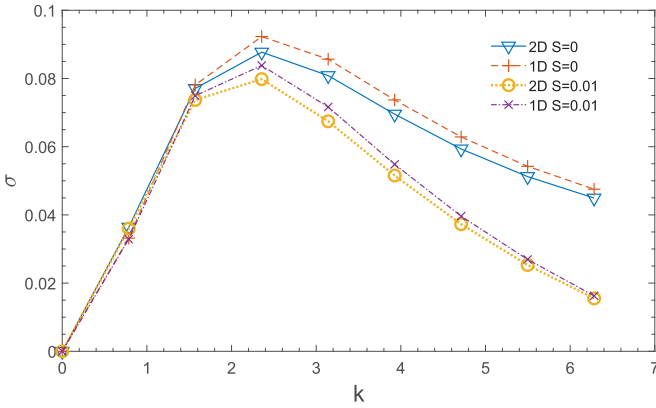


FIG. 4. Growth rate instability as a function of the wave number, for  $A_\rho = A_\mu = 0.6$ ,  $L_s = 0.01$ ,  $H = 1$ ,  $S = 0$ , and  $S = 0.01$ .

numerical approaches to the simulation of the VRTI are normally limited to visually correct snapshots of the flow evolution and the confirmation of the robustness and speed of the multiphase formulation. Very few SPH approaches [23,40] contain a detailed quantitative comparison to other classical numerical formulations where well-established results such as the growth rate of the linear part of the VRTI are monitored. Consequently, the objective of this section is not only to present the results of the SPH formulation, but also to compare the initial evolution of the SPH solution with the results

presented by the 1D spectral and the 2D finite element validated formulations in terms of growth rate. The comparison will be performed for a wide range of Atwood and wave numbers, with and without surface tension.

To perform this task, a fixed point with coordinates  $(x, y) = (0, H/10)$ , is selected to monitor the evolution of the interpolated velocity of the surrounding particles. To trigger the VRTI, an initial perturbation  $\hat{v}_0(x, y)$  of magnitude  $\epsilon \ll \sqrt{gH}$  is added to the initial flow. This perturbation is horizontally periodic with a wave number  $k$  and exponentially decaying on the vertical axis, and consequently we expect to trigger the instability associated with that particular wave number. The expression of the initial vertical velocity perturbation is

$$\hat{v}_0(x, y) = \epsilon \cos(kx) \exp\left(-\left|\frac{y}{(y+H)(y-H)}\right|\right). \quad (47)$$

In Fig. 6 a snapshot of the evolution of the pressure, density and velocity fields is shown at time  $t/t_0 = 5$ , when the initial flow is excited with  $k = \pi$  and both Atwood numbers are equal,  $A_\rho = A_\mu = 0.6$ . At this time step, the velocity field is immersed in the linear regime after the initial oscillations caused by the combination of the particle setup and the weakly compressible assumption. It is worth noting that the velocity perturbations correspond to the most unstable mode obtained after the linear stability analysis (see Fig. 5), matching well the velocity snapshots of the SPH simulation. Pressure and density include the nonzero initial field and consequently are not directly comparable.

An example of the time evolution of the velocity for the case with  $A_\rho = A_\mu = 0.6$  and wave numbers  $k = 3\pi/4$  and  $k = \pi$  is shown in Fig. 7. As can be seen, at the beginning the initial perturbation is hidden behind the noise created by the pressure field trying to satisfy the weakly compressible assumption, which creates a few oscillations. Once the particles have settled down and the pressure field stabilizes  $t/t_0 \sim 1.5$ , the perturbation triggers the VRTI and the system evolves in time with a clean, growing linear regime. As can be observed in the figure, the slope of this signal is parallel to the growth rate computed by the linear stability analysis, which indicates excellent matching with the linear theory.

A complete comparison between the growth rates obtained from the transient slopes of the SPH simulations and the corresponding values obtained from the linear stability analysis is shown in Fig. 8. The comparison is performed using eight wave numbers in the interval  $k \in [0, 2\pi]$  and four density-viscosity Atwood numbers  $A_\rho = A_\mu = 0.2, 0.4, 0.6, 0.8$ . With the exception of a very few points obtained for the largest Atwood number, the agreement obtained is reasonable and the maximum of each curve is always detected at  $k \approx 3\pi/4$ . The detection and identification of the slopes of the linear intervals during the SPH simulation is a numerically sensitive task that can also be considered a source of error.

Figure 9 represents what occurs when the wave number of the initial perturbation  $k = \pi/4$  is not close to the wave number  $k_{max} \approx 3\pi/4$  that gives the maximum growth rate of the instability. After the adaptation interval, three clearly distinguishable slopes are present with a transient between them showing that the dynamical evolution of the linear system jumps from the perturbed mode to the next most unstable

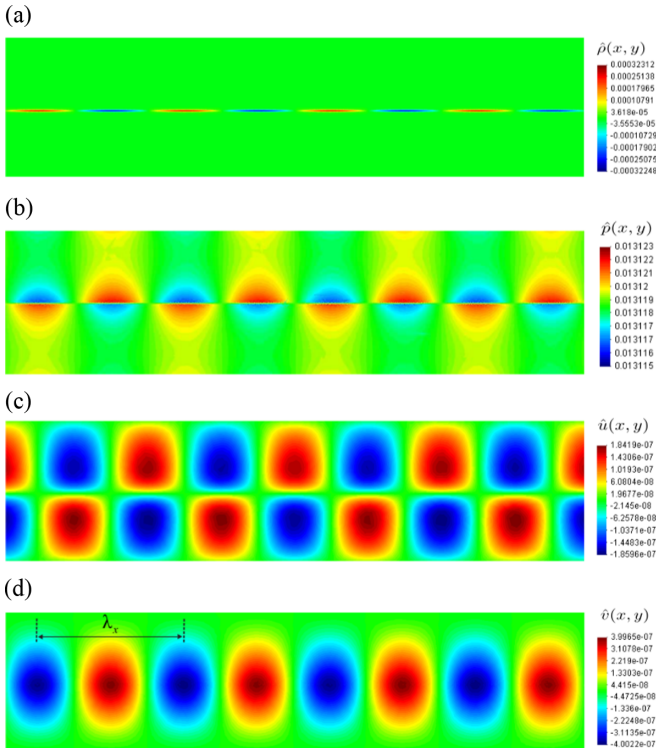


FIG. 5. Perturbation amplitude for the case  $k = \pi$ ,  $2H = 2$ ,  $2L = 8$ ,  $A_\mu = A_\rho = 0.2$ , and  $S = 0.003$ . From top to bottom the amplitude perturbations are represented for the density (a), pressure (b), horizontal velocity (c), and vertical velocity (d). All computations were performed using the interface parameter  $L_s = 0.01$ .

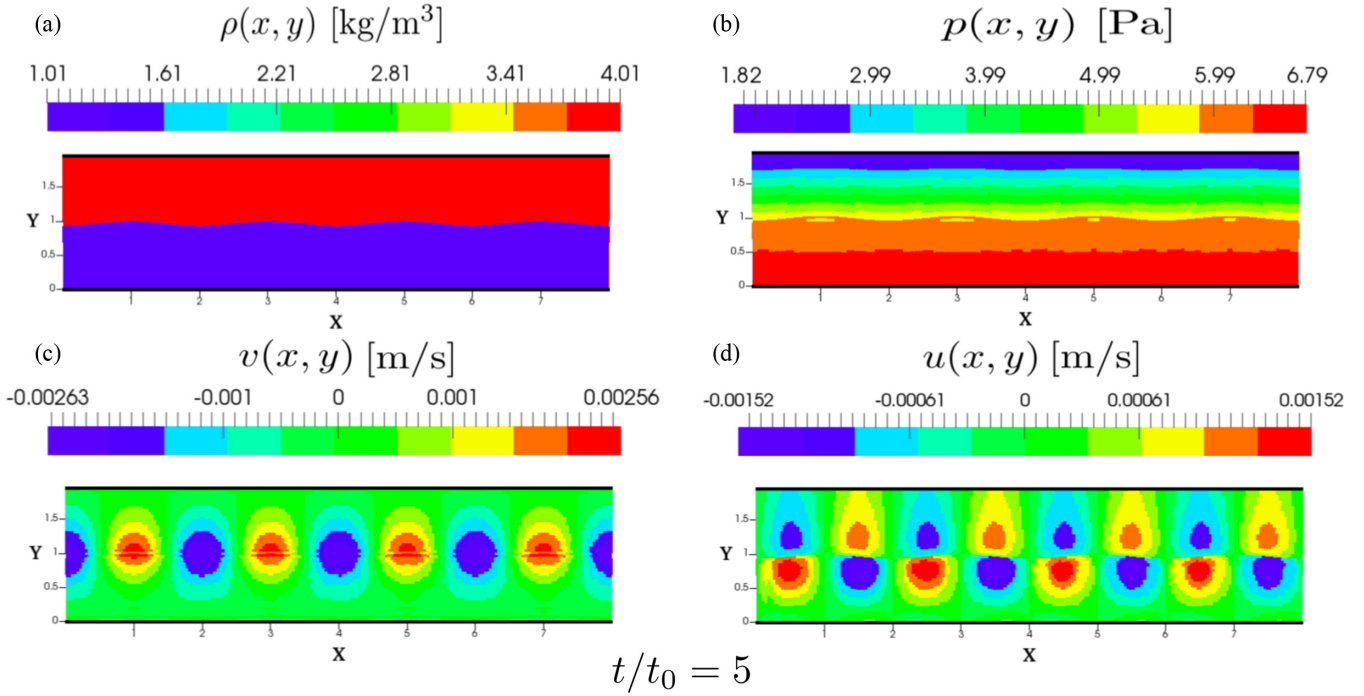


FIG. 6. Snapshots of the SPH simulation at  $t/t_0 = 5$  for the case  $k = \pi$ ,  $2H = 2$ ,  $2L = 8$ , and  $A_\mu = A_\rho = 0.6$ . The 2D fields are represented for the density (a), pressure (b), vertical velocity (c), and horizontal velocity (d).

mode until it reaches  $k_{\max}$ . The first slope matches the growth rate of the initial excitation  $k = \pi/4$ , but around time  $t/t_0 \sim 7.4$ , the system evolves to the second mode with  $k = \pi/2$ , and then at  $t/t_0 \sim 12$  it finally jumps to the wave number that gives the maximum growth rate at  $k = k_{\max} = 3\pi/4$ .

In Fig. 10 the growth rate of the perturbation is represented against the density Atwood number  $A_\rho \in [0.1, 0.9]$  for the case  $2H = 2$ ,  $2L = 8$  and  $k = 3\pi/4$ , being the viscosity equal to 1 in both phases and consequently  $A_\mu = 0$ . As can be appreciated, the agreement with the results presented in [10] is excellent. A similar computation is performed in the same Atwood range but in this case  $A_\rho = A_\mu$  and  $k = 3\pi/4$ , and the results predicted by SPH approximate the linear stability calculations well.

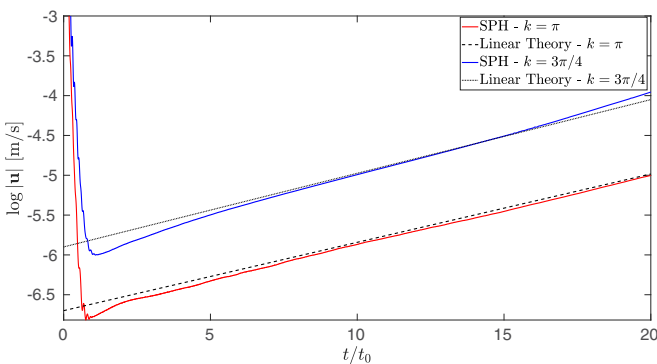


FIG. 7. Comparison of the evolution of the velocity at  $(x, y) = (0, H/10)$  when the SPH simulations are compared to the linear stability analysis results represented by the dotted lines for  $A_\rho = A_\mu = 0.6$  and  $k = \pi$  (red) and  $k = 3\pi/4$  (blue).

When the SPH surface tension model described in Sec. III B is added to the problem, the SPH results still obtain a good prediction and capture the instability reduction due to the surface tension contribution; see Fig. 11. Alternatively, a second simplified implementation of the surface tension based on Eqs. (19), (23), and (24) was also performed in SPH. Combining those equations, we can consider that the presence of surface tension is equivalent to a gravity reduction given by the equation

$$g_s = g \left( 1 - \frac{k^2 S}{A_\rho} \right), \quad (48)$$

where  $g_s$  is the gravity value when the surface tension  $S$  is included in the model and the second derivative has been

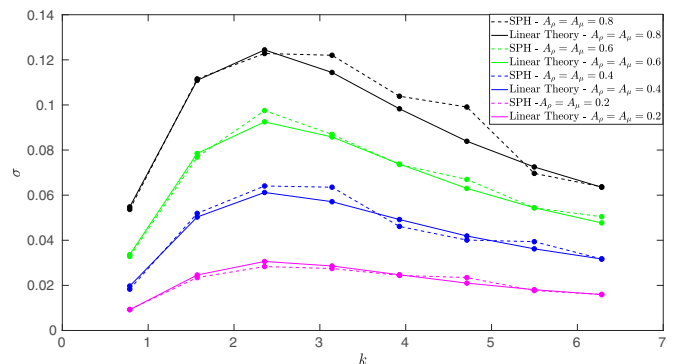


FIG. 8. Growth rate of the vertical velocity at the fixed point  $x = 0$ ,  $y = H/10$  versus wave number for different values of the density and viscosity Atwood numbers  $A_\rho = A_\mu$ ,  $2H = 4$ , and  $2L = 1$ . The growth rate is compared to the values predicted by the linear stability analysis theory [10].



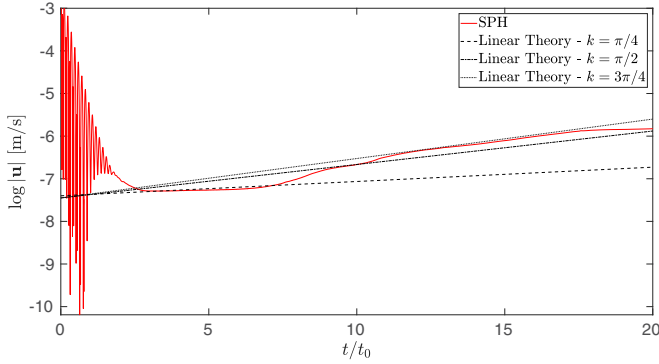


FIG. 9. Comparison of the evolution of the velocity at  $(x, y) = (0, H/10)$  when the initial state of the SPH simulation is perturbed with  $k = \pi/4$ . Results are compared to three reference results of the linear stability analysis represented by the dotted lines for  $A_\rho = A_\mu = 0.6$  and  $k = \pi/4, \pi/2$ , and  $3\pi/4$ .

replaced by  $-k^2$  assuming during this linear stage a horizontal periodicity of the flow with the same wave number as the initial excitation. This simplification is valid only for comparing the results during the linear regime also computed by the stability analysis, and no realistic results are expected during the nonlinear evolution of the SPH simulation. However, the results obtained by this simplified implementation of the sur-

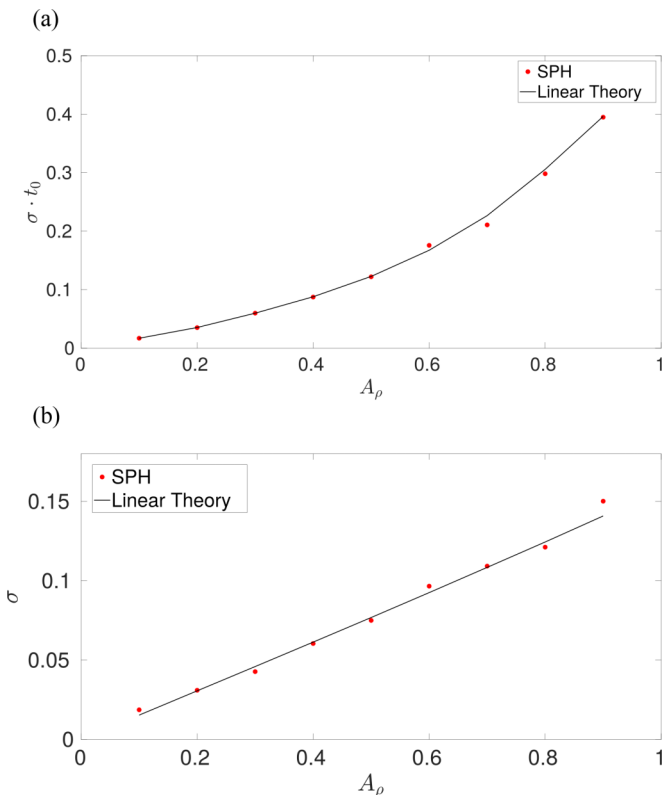


FIG. 10. Growth rate versus density Atwood number obtained in a computational domain  $2H = 8, 2L = 2$ . (a)  $A_\mu = 0$  and  $k = \pi/4$ ; note that since  $A_\mu = 0$  the growth rate  $\sigma$  has to be adimensionalized with  $t_0$ . (b)  $A_\mu = A_\rho$ , and  $k = 3\pi/4$ . The values predicted by Ref. [10] are also plotted for comparison.

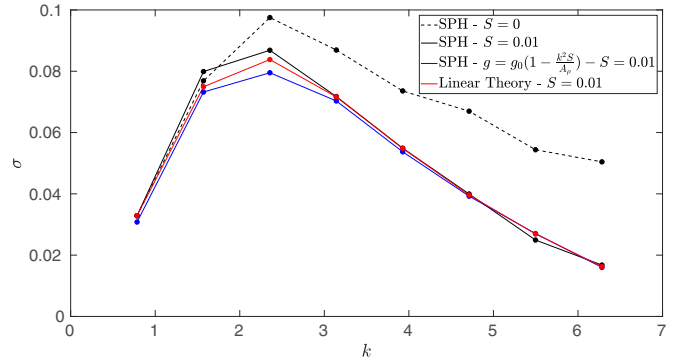


FIG. 11. Growth rate versus wave number for  $A_\rho = A_\mu = 0.6$  with and without surface tension. The growth rate is compared to the values predicted by the linear stability analysis theory.

face tension approximate the ones from the linear theory very well, with little underprediction for the largest growth rate.

In Fig. 11 the case without surface tension has been added to the graph to observe the stability decreases for large wave numbers when surface tension is present, showing that the surface tension has a stabilizing effect on the VRTI.

### B. VRTI in a confined tank with no-slip lateral boundary conditions

#### 1. Linear stability analysis

In this section the same linear stability analysis that has been performed in Sec. IV A 1 with periodic boundary conditions is now solved with no-slip velocity boundary conditions in the right and left boundaries at  $x = \pm L$ ; see the bottom part of Fig. 1. As a nonperiodic assumption is allowed in the horizontal direction, the results of this analysis cannot be computed anymore using the classical 1D spectral stability analysis (see [16]) and can be performed only using a 2D formulation. In Figs. 12 and 13 the spectrum obtained in this no-slip case is compared to the previous periodic case for two different geometries, the first one being  $(2H, 2L) = (2, 8)$  and the second being  $(2H, 2L) = (4, 1)$ . As can be observed, the

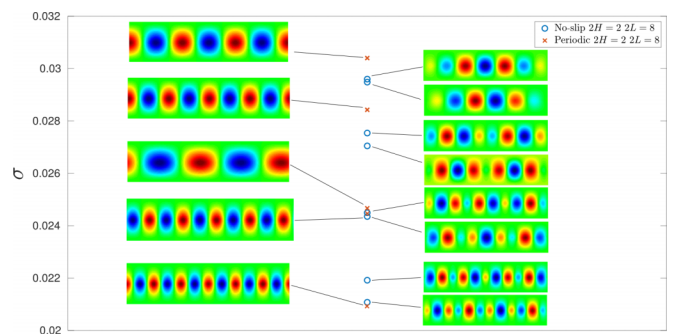


FIG. 12. Comparison of the spectrum and the vertical velocity perturbations associated to the most unstable eigenvalues when periodic and homogeneous no-slip lateral boundary conditions are used for  $A_\rho = A_\mu = 0.2, 2H = 2$ , and  $2L = 8$ .

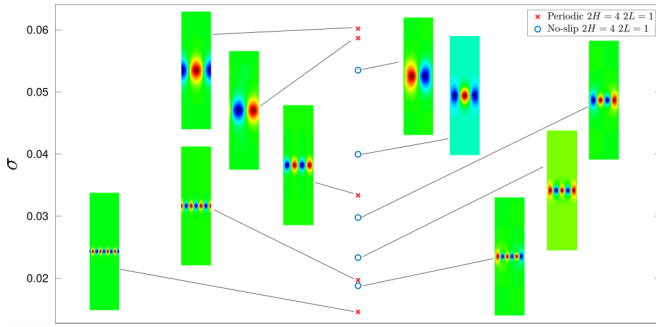


FIG. 13. Comparison of the spectrum and the vertical velocity perturbations associated with the most unstable eigenvalues when periodic and homogeneous no-slip lateral boundary conditions for  $A_p = 0.7621$ ,  $A_\mu = 0$ ,  $2H = 4$ , and  $2L = 1$ .

values of the most unstable modes and the vertical velocity perturbation associated with those eigenvalues clearly transformed when the lateral boundary conditions are changed. As expected, the velocity modes associated with the confined case studied in this section satisfy the no-slip boundary conditions imposed, and the modes are attenuated close to the lateral walls.

An important observation when no slip boundary conditions are used in a domain with horizontal fixed length is that we cannot assume a clear spatial periodicity in the horizontal direction, and consequently no wave number can be associated with the different modes. This clearly indicates that changing the lateral boundary conditions implies the absence of horizontal periodicity.

**2. SPH simulation of the VRTI in a confined tank**

In this section, the SPH formulation will be applied to the tank case. Despite having shown in the previous section that when lateral boundaries are changed to no-slip no clear wave number is identified in the eigenvectors of the linear stability analysis, and an approximate wave number is necessary to build the initial condition of the SPH problem. In order to compare this with the linear stability analysis (see Figs. 12 and 13), the base flow is excited according to the following expression:

$$\hat{v}_0(x, y) = \epsilon \sin(kx) \exp\left(-\left|\frac{y}{(y+H)(y-H)}\right|\right), \quad (49)$$

where the initial perturbation  $\hat{v}_0$  has been selected in order to satisfy the no-slip boundary condition at  $x = \pm L$ .

In Fig. 14 the growth rates obtained measuring the slope of the linear velocity growth at  $(x, y) = (0, H/10)$  are compared, for different Atwood numbers, to the most unstable eigenvalue obtained from the linear analysis of both geometries previously analyzed in Sec. IV B 1. For the sake of simplicity, both the viscosity and density Atwood numbers were equal,  $A_p = A_\mu$ . As can be observed, excellent agreement is obtained for all Atwood numbers. In order to confirm the reduction in terms of growth rate, the previous results with periodic boundary conditions are also plotted in Fig. 14. As expected from the comparison performed using the linear

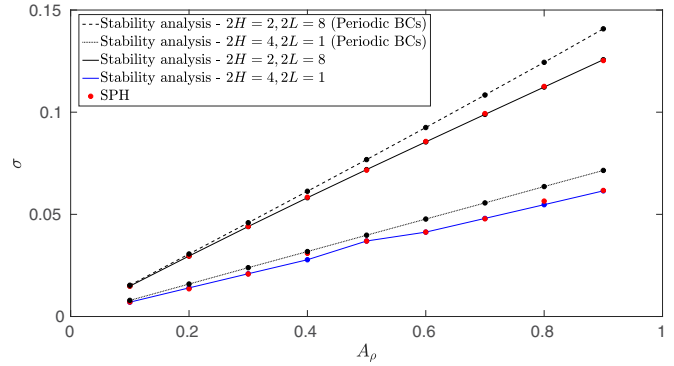


FIG. 14. Growth rate of the vertical velocity at the fixed point  $(x, y) = (0, H/10)$  for different values of the density and viscosity Atwood numbers  $A_\mu = A_p$ ,  $2H = 2$  and  $4$ ,  $2L = 8$  and  $1$ . The growth rate is compared to the values predicted by the linear stability analysis theory.

stability analysis in Figs. 12 and 13, the linear part presents a lower growth rate (smaller eigenvalue) than the periodic version. We conclude that the presence of the lateral walls decreases the growth rate of the VRTI as they increase the viscous action.

**V. CONCLUSIONS**

The most important conclusions obtained in this work are the following:

- (1) The RTI instability has been numerically studied in 2D with regularized density and viscosity according to a hyperbolic tangent function. The Navier-Stokes equations are linearized and discretized using the finite element method, and the final generalized eigenvalue problem obtained is solved using the Arnoldi method. The model introduces the possibility of confining the fluid either in the vertical or horizontal directions, adding viscosity to both phases and introducing surface tension to the interface.
- (2) The classical 1D formulation is limited to those cases where the horizontal coordinate is periodic, in contrast with the 2D formulation assumed here, which permits studying more general cases, as, for example, those cases where the fluids are confined and no-slip boundary conditions are necessary for the lateral walls. This situation appears in engineering applications as a Rayleigh-Taylor instability, which is frequently found in accelerating fuel tanks.
- (3) The VRTI instability has been also been simulated with a Lagrangian particle method called the multiphase WC-SPH. This method is clearly nonlinear but is able to capture the linear regime that is present at the first stage of the simulation. The multiphase SPH formulation presents a robust stability for a wide range of densities and viscosities, gives the possibility of implementing both the no-slip and the periodic boundary conditions, and contains a surface tension model for the interface.
- (4) The matching between both formulations is very good in a relevant range of wave numbers, indicating that a Lagrangian formulation not only is able to predict the growth rate values and the corresponding structures identified with

the eigenvalues and the eigenvectors of the generalized LNSE, but also captures the evolution of the internal dynamics of the different growing modes involved in the Rayleigh-Taylor instability.

(5) Both formulations were also compared with the results provided in [10] obtaining very good agreement for a wide range of density and viscosity ratios.

(6) The 2D formulation allows for performing the same analysis in geometries more complex than the simple rectangular tank used here, or even in realistic baffled fuel tanks like the ones used in the aircraft industry.

## ACKNOWLEDGMENTS

The research leading to these results was undertaken as part of the SLOWD project, which has received funding from the European Union's Horizon 2020 research and innovation programme under Grant No. 815044. L.M.G. acknowledges the financial support from the Spanish Ministry for Science, Innovation and Universities (MCIU) under Grant No. RTI2018-096791-B-C21, Hidrodinámica de elementos de amortiguamiento del movimiento de aerogeneradores flotantes. All the authors would like to thank Mr. Ciaran Stone for his valuable assistance during the preparation of this manuscript.

- 
- [1] O. M. Faltinsen and A. N. Timokha, *Sloshing* (Cambridge University Press, Cambridge, 2009).
- [2] L. Rayleigh, Investigation of the character of the equilibrium of an incompressible heavy fluid of variable density, *Proc. London Math. Soc.* **s1-14**, 170 (1883).
- [3] G. I. Taylor, Instability of liquid surfaces when accelerated in a direction perpendicular to their planes, *Proc. R. Soc. London* **201**, 192 (1950).
- [4] R. E. Rosensweig, Y. Hirota, S. Tsuda, and K. Raj, Study of audio speakers containing ferrofluid, *J. Phys.: Condens. Matter* **20**, 204147 (2008).
- [5] C. Harig, P. Molnar, and G. A. Houseman, Rayleigh-Taylor instability under a shear stress free top boundary condition and its relevance to removal of mantle lithosphere from beneath the Sierra Nevada, *Tectonics* **27**, TC6019 (2008).
- [6] T. M. Willey, K. Champley, R. Hodgkin, L. Lauderbach, M. Bagge-Hansen, C. May, N. Sanchez, B. J. Jensen, A. Iverson, and T. van Buuren, X-ray imaging and 3D reconstruction of in-flight exploding foil initiation flyers, *J. Appl. Phys.* **119**, 235901 (2016).
- [7] T. G. Theofanous, Aerobreakup of Newtonian and viscoelastic liquids, *Annu. Rev. Fluid Mech.* **43**, 661 (2011).
- [8] A. A. Blinova, M. M. Romanova, and R. V. E. Lovelace, Boundary between stable and unstable regimes of accretion. ordered and chaotic unstable regimes, *Mon. Not. R. Astron. Soc.* **459**, 2354 (2016).
- [9] A. Tavakoli, L. Hadzievski, and D. D. Tskhakayab, Rayleigh-Taylor instability of magnetized density transition layer, *Phys. Plasmas* **7**, 89 (1999).
- [10] K. O. Mikaelian, Rayleigh-Taylor instability in finite-thickness fluids with viscosity and surface tension, *Phys. Rev. E* **54**, 3676 (1996).
- [11] M. H. O. Allah, Effects of stratification, surface tension and rigid planes on Rayleigh-Taylor instability, *Ind. J. Pure Appl. Math.* **32**, 303 (2001).
- [12] R. V. Morgan, O. A. Likhachev, and J. W. Jacobs, Rarefaction-driven Rayleigh-Taylor instability I: Diffuse-interface linear stability measurements and theory, *J. Fluid Mech.* **791**, 34 (2016).
- [13] R. E. Duff, F. H. Harlow, and C. W. Hirt, Effects of stratification, surface tension and rigid planes on Rayleigh-Taylor instability, *Phys. Fluids* **5**, 417 (1962).
- [14] C. X. Yu, C. Xue, J. Liu, X. Y. Hu, Y. Y. Liu, W. H. Ye, L. F. Wang, J. F. Wu, and Z. F. Fan, Multiple eigenmodes of the Rayleigh-Taylor instability observed for a fluid interface with smoothly varying density, *Phys. Rev. E* **97**, 013102 (2018).
- [15] M. Dong, Z. Fan, and C. Yu, Multiple eigenmodes of the Rayleigh-Taylor instability observed for a fluid interface with smoothly varying density. II. Asymptotic solution and its interpretation, *Phys. Rev. E* **99**, 013109 (2019).
- [16] L. M. González-Gutiérrez and A. de Andrea González, Numerical computation of the Rayleigh-Taylor instability for a viscous fluid with regularized interface properties, *Phys. Rev. E* **100**, 013101 (2019).
- [17] I. Hammani, S. Marrone, A. Colagrossi, G. Oger and D. Le Touzé, Detailed study on the extension of the  $\delta$ -SPH model to multi-phase flow, *Computer Methods in Applied Mechanics and Engineering* **368**, 113189 (2020).
- [18] S. J. Cummins and M. Rudman, An SPH projection method, *J. Comput. Phys.* **152**, 584 (1999).
- [19] A. M. Tartakovsky and P. Meakin, A smoothed particle hydrodynamics model for miscible flow in three-dimensional fractures and the two-dimensional Rayleigh-Taylor instability, *J. Comput. Phys.* **207**, 610 (2005).
- [20] N. Grenier, M. Antuono, A. Colagrossi, D. Le Touzé, and B. Alessandrini, An Hamiltonian interface SPH formulation for multi-fluid and free surface flows, *J. Comput. Phys.* **228**, 8380 (2009).
- [21] K. Szewc, A. Tanière, and J.P. Minier, A study on application of smoothed particle hydrodynamics to multi-phase flows, *Int. J. Nonlinear Sci. Numer. Simul.* **13**, 383 (2012).
- [22] Mostafa Safdari Shadloo and Mehmet Yildiz, ISPH Modelling of Rayleigh-Taylor Instability, in *Congress: 6th International SPHERIC Workshop* (Hamburg, Germany, 2011).
- [23] M. Shadloo, A. Zainali, and M. Yildiz, Simulation of single mode Rayleigh-Taylor instability by SPH method, *Comput. Mech.* **51**, 699 (2013).
- [24] R. Hide, The character of the equilibrium of a heavy, viscous, incompressible, rotating fluids of variable density. I. General theory, *Q. J. Mech. Appl. Math.* **9**, 22 (1955).
- [25] S. Chandrasekhar, *Hydrodynamic and Hydromagnetic Stability* (Dover, New York, 1981).
- [26] L. M. González, V. Theofilis, and R. Gómez-Blanco, Finite-element numerical methods for viscous incompressible

- BiGlobal linear instability analysis on unstructured meshes, *AIAA J.* **45**, 840 (2007).
- [27] V. Theofilis, Advances in global linear instability analysis of nonparallel and three-dimensional flows, *Prog. Aerosp. Sci.* **39**, 249 (2003).
- [28] V. Theofilis, P. W. Duck, and J. Owen, Viscous linear stability analysis of rectangular duct and cavity flows, *J. Fluid. Mech.* **505**, 249 (2004).
- [29] Y. Saad, Variations of Arnoldi's method for computing eigenvalues of large unsymmetric matrices, *Linear Algebra Appl.* **34**, 269 (1980).
- [30] J. L. Cercos-Pita, AQUAgpusph, a new free 3D SPH solver accelerated with OpenCL, *Comput. Phys. Commun.* **192**, 295 (2015).
- [31] M. Antuono, A. Colagrossi, and S. Marrone, Numerical diffusive terms in weakly-compressible SPH schemes, *Comput. Phys. Commun.* **183**, 2570 (2012).
- [32] P. W. Randles and L. D. Libersky, Smoothed particle hydrodynamics: Some recent improvements and applications, *Comput. Methods Appl. Mech. Eng.* **139**, 375 (1996).
- [33] M. Antuono, S. Marrone, A. Colagrossi, and B. Bouscasse, Energy balance in the  $\delta$ -SPH scheme, *Comput. Methods Appl. Mech. Eng.* **289**, 209 (2015).
- [34] M. Antuono, A. Colagrossi, S. Marrone, and D. Molteni, Free-surface flows solved by means of SPH schemes with numerical diffusive terms, *Comput. Phys. Commun.* **181**, 532 (2010).
- [35] J. P. Morris, Simulating surface tension with smoothed particle hydrodynamics, *Int. J. Numer. Methods Fluids* **33**, 333 (2000).
- [36] M. Ferrand, D. R. Laurence, B. D. Rogers, D. Violeau, and C. Kassiotis, Unified semi-analytical wall boundary conditions for inviscid laminar or turbulent flows in the meshless SPH method, *Int. J. Numer. Methods Fluids* **71**, 446 (2013).
- [37] J. Calderon-Sanchez, J. L. Cercos-Pita, and D. Duque, A geometric formulation of the Shepard renormalization factor, *Comput. Fluids* **183**, 16 (2019).
- [38] J. Feldman and J. Bonet, Dynamic refinement and boundary contact forces in SPH with applications in fluid flow problems, *Int. J. Numer. Methods Eng.* **72**, 295 (2007).
- [39] L. Chiron, M. De Lefte, G. Oger, and D. Le Touzé, Fast and accurate SPH modelling of 3D complex wall boundaries in viscous and non viscous flows, *Comput. Phys. Commun.* **234**, 93 (2019).
- [40] A. Rahmat, N. Tofighi, M. S. Shadloo, and M. Yildiz, Numerical simulation of wall bounded and electrically excited Rayleigh–Taylor instability using incompressible smoothed particle hydrodynamics, *Colloids Surf. A* **460**, 60 (2014).